Beyond Ensembles: Simulating All-Atom Protein Dynamics in a Learned Latent Space

Aditya Sengar^{1,2,†} Jiying Zhang² Pierre Vandergheynst¹ Patrick Barth^{2,3} September 26, 2025

Preprint

Signal Processing Laboratory (LTS2), EPFL, Lausanne, Switzerland
 Institute of Bioengineering, EPFL, Lausanne, Switzerland
 Ludwig Institute for Cancer Research, Lausanne, Switzerland
 † Corresponding author: aditya.sengar@epfl.ch

Abstract

Simulating the long-timescale dynamics of biomolecules is a central challenge in computational science. While enhanced sampling methods can accelerate these simulations, they rely on pre-defined collective variables that are often difficult to identify. A recent generative model, LD-FPG, demonstrated that this problem could be bypassed by learning to sample the static equilibrium ensemble as all-atom deformations from a reference structure, establishing a powerful method for all-atom ensemble generation. However, while this approach successfully captures a system's probable conformations, it does not model the temporal evolution between them. We introduce the Graph Latent Dynamics Propagator (GLDP), a modular component for simulating dynamics within the learned latent space of LD-FPG. We then compare three classes of propagators: (i) score-guided Langevin dynamics, (ii) Koopman-based linear operators, and (iii) autoregressive neural networks. Within a unified encoder—propagator—decoder framework, we evaluate long-horizon stability, backbone and side-chain ensemble fidelity, and functional free-energy landscapes. Autoregressive neural networks deliver the most robust long rollouts; score-guided Langevin best recovers side-chain thermodynamics when the score is well learned; and Koopman provides an interpretable, lightweight baseline that tends to damp fluctuations. These results clarify the trade-offs among propagators and offer practical guidance for latent-space simulators of all-atom protein dynamics.

1 Introduction

Molecular simulations are indispensable for studying the complex dynamics that govern biological function, yet brute-force approaches struggle to access the slow, functionally relevant motions—such as protein folding, ligand binding, or allosteric switching—due to rugged energy landscapes and the dominance of rare events [1, 2]. To mitigate this gap—beyond what enhanced sampling can offer when suitable collective variables are hard to specify [3] —a complementary strategy has gained traction: recasting the simulation challenge from one of brute-force integration to one of representation learning. In this *representation-first* view, the simulation problem is recast as a modular encoder–propagator–decoder pipeline: an encoder maps high-dimensional atomic configurations into a continuous, low-dimensional latent space; a propagator evolves the system's state within this simplified space; and a decoder maps the resulting latent trajectory back to all-atom coordinates [4, 5].

Progress in this paradigm follows two complementary directions: The first focuses on learning the underlying physics, employing score-based diffusion [6, 7], flow matching [8], and energy-based models

[9] to learn generative surrogates—sometimes yielding differentiable force fields—that implicitly define the system's potential of mean force [10, 11, 12, 13]. The second centers on learning simplified dynamical coordinates, using time-aware autoencoders or Koopman/DMD analysis [14, 15] to discover an intrinsic manifold where the long-term dynamics become stable, predictable, or even approximately linear [16, 17, 18, 19, 20].

Despite the promise of latent-space simulation, the choice of propagator—the engine that advances the state—entails a trade-off between physical faithfulness, long-horizon stability, and expressive capacity. We adopt LD-FPG [21] as a fixed encoder—decoder and compare, in the same latent, three propagators: (i) score-guided Langevin dynamics, (ii) a Koopman linear operator, and (iii) an autoregressive neural network (NN). Our analysis reveals a clear trade-off: the MLP is most stable, the score-guided model is most physically detailed for local motions, and the Koopman operator is a simple but overly rigid baseline.

Contributions: (1) A controlled study that holds the LD-FPG encoder–decoder fixed while swapping the latent propagator, isolating where gains arise.(2) Three propagators within one latent: score-guided Langevin, a Koopman operator, and an autoregressive NN.(3) Benchmarks on alanine dipeptide, 7JFL, and A_1AR .(4) First learned, all-atom rollout (to our knowledge) that recovers a GPCR activation surface (A_2AR).

2 Related Work

The encoder–propagator–decoder blueprint. Simulating in a low-dimensional space is well established. Molecular Latent Space Simulators (LSS) [4] and Deep Generative MSMs (DeepGenMSM) [5] factorize the task into an encoder that maps coordinates to latent variables, a propagator that advances them, and a decoder that returns all-atom structures. Realizations include autoregressive simulators with recurrent propagators [22], trajectory-level generators that synthesize MD clips in coordinate space [23], LSS variants that target free-energy surfaces and transition kinetics [24], and joint conformation–dynamics models trained via autoregression [25]. We follow this modular design but (i) *hold the LD-FPG decoder fixed* to control reconstruction quality and (ii) focus our analysis on the choice of latent propagator.

Learning dynamically aware latent spaces (encoders). The quality of a latent simulation hinges on the quality of the latent space itself. While linear methods like time-lagged independent component analysis (TICA) remain strong baselines for identifying slow variables [26], deep learning has enabled far more expressive encoders. Time-lagged autoencoders such as the Variational Dynamics Encoder (VDE) learn non-linear representations predictive over a time delay Δt [16, 27]. VAMPnets use a variational principle to approximate the leading Koopman eigenfunctions, corresponding to the slowest dynamical processes [17]. To remove hand-crafted features, modern approaches leverage graph neural networks (GNNs) to learn CVs directly from coordinates in a permutation- and symmetry-aware manner [28, 20, 29], often with information-bottleneck objectives to explicitly optimize predictiveness of future states [30]. For a recent overview of time-lagged encoders and related autoencoder variants, see [31].

Linear dynamics in latent space (Koopman/DMD propagators). The Koopman-operator framework provides a route to linearize non-linear dynamics in a learned observable space [18]. Extended dynamic mode decomposition (EDMD) [32] and DMD [15] showed that a wide class of systems admits accurate linear predictors; subsequent work learns such observables end-to-end with deep encoders [14]. This has inspired Koopman autoencoders that enforce a linear evolution rule within the latent space [19, 33, 34], often yielding strong long-horizon stability by reducing compounding errors in nonlinear rollouts. Beyond linear Koopman rules, implicit transfer-operator learning uses a diffusion model to parameterize the Markov kernel at multiple lags, yielding consistent long-horizon rollouts under SE(3) symmetry [35].

Non-linear sequence models (neural propagators). A complementary path directly learns the non-linear transition function. The Learning Effective Dynamics (LED) framework uses LSTMs to propagate latent variables and capture memory effects [22]; others pair RNNs with physical resampling such as Maximum Caliber to enforce kinetic consistency [36]. Continuous-time learners (Neural ODEs) offer flexible parametric flows [37], with extensions to stochastic settings via Neural SDEs [38]. Recent work also couples an autoregressive temporal module with an SE(3)-equivariant diffusion decoder to jointly learn conformations and their ordering from MD (ConfRover) [25]. Our MLP propagator serves as a streamlined baseline in this family.

Physics-guided stochastic models (Langevin and diffusion). Generative models increasingly embed statistical-mechanics structure. Score-based diffusion has been used to learn effective force fields for coarse-grained MD [10], tying the denoising objective to forces and Langevin-type simulators via the SDE view of score models [6]. For accelerated evolution, *frame-to-frame* diffusion/score surrogates have been proposed, including DiffMD for trajectory synthesis conditioned on the previous frame [39] and Score Dynamics, which targets picosecond time steps while preserving short-time kinetic signals [12]. Flow-matching has likewise been applied to coarse-grained rollouts without explicit forces (F³low; manifold/SE(3)-equivariant) [13] and to learning coarse-grained free-energy models via density estimation [40]. A recurring theme is *consistency* between the sampled equilibrium ensemble and the stationary law of the learned dynamics; enforcing Fokker–Planck consistency during training improves long-horizon behavior [11].

GPCRs as a proving ground for slow dynamics. G protein-coupled receptors (GPCRs) are a demanding testbed for dynamic models, as their function is governed by slow transitions between metastable states [1, 2]. Decades of structural and computational work have characterized the micro-switches and allosteric pathways involved in their activation [41, 42], making them ideal systems for benchmarking. Our evaluation on A_1AR and A_2AR tests the ability of each latent propagator to recover these functionally critical motions.

Positioning among recent generative simulators. While geometric diffusion models achieve strong results for static 3D structures and poses [43, 44], our focus is the distinct problem of simulating temporal dynamics. Recent efforts include coordinate-space trajectory synthesis with diffusion (GeoTDM) [45], SE(3)-equivariant flow matching for frame-to-frame coarse-grained rollouts (F³low) [13], and neural operators for multi-step 3D dynamics (EGNO) [46]. In parallel, latent and physics-informed approaches aim to accelerate sampling or encode structure—LAST for adaptive MD [47], ConfRover for joint conformation—dynamics learning [25], and NeuralMD, a multi-grained group-symmetric differential-equation model for protein—ligand binding dynamics [48]. Complementing these directions, we isolate the *propagator* by comparing linear (Koopman), neural, and score-guided dynamics *within the same learned latent and fixed decoder*, enabling a controlled comparison of long-horizon stability, ensemble fidelity, and functional free-energy surfaces.

3 Methods

GLDP extends the LD-FPG encoder–decoder backbone [21] (see App. A.2) by adding a temporal propagator that operates entirely within the LD-FPG latent. The encoder–decoder is kept fixed (frozen) in all experiments; only the propagator is swapped.

3.1 GLDP: Propagation in the LD-FPG Latent Space

We adopt the LD-FPG encoder–decoder backbone. The encoder, a Chebyshev Graph Neural Network (ChebNet), maps all-atom coordinates $X(t) \in \mathbb{R}^{N \times 3}$ to a pooled latent $z(t) \in \mathbb{R}^d$. Trained on an MD

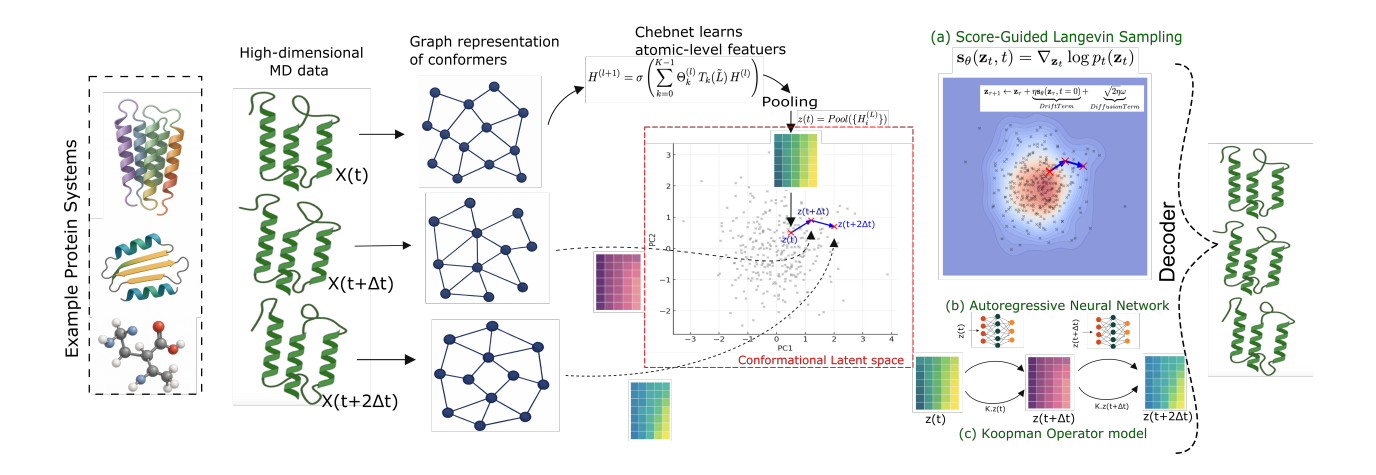


Figure 1: **Framework overview.** A pre-trained LD-FPG encoder (ChebNet; left) maps all-atom coordinates X(t) to a pooled latent z(t). Within the fixed LD-FPG latent, GLDP advances the state via one of three propagators (red box): (a) score-guided Langevin using the LD-FPG denoiser to estimate $s_{\theta}(z,\tau) = \nabla_z \log p_{\tau}(z)$ at a fixed low-noise level; (b) an autoregressive NN $z_{t+1} = f_{\theta}(z_t)$; and (c) a Koopman linear operator $z_{t+1} = Az_t$. The frozen LD-FPG decoder (right) maps the latent trajectory back to all-atom structures $\hat{X}(t + \Delta t)$.

trajectory, the encoder produces a time series $\{z_0, z_1, \dots, z_M\}$ that captures conformational variation. We then learn a latent-time update of the form

$$z_{t+1} = f(z_t) + \eta_t, \qquad \eta_t \sim \mathcal{N}(0, \sigma_\eta^2 I), \tag{1}$$

where f is the propagator and η_t is optional rollout noise. Unless noted, training pairs use a one-frame stride (z_t, z_{t+1}) , latents are standardized per dimension using training-set statistics before fitting the propagator (and unstandardized before decoding), and the initial state \hat{z}_0 is the encoding of a held-out MD frame. Key notation appears in Table 10; a glossary is in Table 11.

3.2 Koopman Propagator via Dynamic Mode Decomposition

The Koopman variant approximates latent evolution with a single linear operator:

$$z_{t+1} \approx A z_t, \qquad A \in \mathbb{R}^{d \times d}.$$

where A is the time-independent Koopman operator that we aim to learn from data. We estimate A with Dynamic Mode Decomposition (DMD) [15]. First, we arrange our latent trajectory into two snapshot matrices, where each column is a state of the system at a point in time,

$$\mathbf{X} = [z_0, \dots, z_{M-2}], \qquad \mathbf{Y} = [z_1, \dots, z_{M-1}],$$

and solve the least-squares map $\min_A \|\mathbf{Y} - A\mathbf{X}\|_F^2$, yielding

$$A = \mathbf{Y}\mathbf{X}^+,$$

where \mathbf{X}^+ is the Moore–Penrose pseudoinverse. For numerical stability and to regularize the model, the pseudoinverse is computed using Singular Value Decomposition (SVD). By truncating the SVD to a lower rank r, we can filter out noise and focus the model on the most energetically significant dynamic modes. Once learned, the operator A is used to generate new trajectories autoregressively from an initial state \hat{z}_0 ; a small Gaussian rollout noise $\eta_t \sim \mathcal{N}(0, \sigma_{\mathrm{koop}}^2 I)$ is added to match the one-step residual variance. Implementation details are provided in App. A.3.

3.3 Autoregressive Neural Network Propagator

To learn the latent transition directly, we use an autoregressive NN. The model parameterizes a deterministic nonlinear map

$$z_{t+1} = f_{\theta}(z_t), \tag{2}$$

trained with a one-step objective over pairs (z_t, z_{t+1}) :

$$\mathcal{L}(\theta) = \frac{1}{M-1} \sum_{t=0}^{M-2} \| f_{\theta}(z_t) - z_{t+1} \|^2.$$
 (3)

To reduce error accumulation in long rollouts, we use dropout and weight decay (see App. A.4 for architecture and training settings). After training, trajectories are generated by iterative application from an initial state \hat{z}_0 :

$$\hat{z}_{i+1} = f_{\theta}(\hat{z}_i) + \eta_i, \qquad \eta_i \sim \mathcal{N}(0, \sigma_{\text{roll}}^2 I), \tag{4}$$

where $\sigma_{\rm roll}$ is chosen on a validation split to match the one-step latent residual variance of $z_{t+1}-z_t$. (Unless noted, \hat{z}_0 is the encoding of a held-out MD frame and latents are standardized per dimension before fitting and unstandardized before decoding.) The network architecture, training procedure, and rollout settings are detailed in Appendix A.4.

3.4 Score-Guided Langevin Propagator

This propagator uses a learned score of the latent equilibrium to define a stochastic simulation. The procedure has two stages.

Stage 1: score model. We train a time-conditional denoiser $\epsilon_{\theta}(z_t, t)$ on latent embeddings with a variance-preserving (VP) schedule as in DDPMs. The forward corruption is

$$z_t = \sqrt{\bar{\alpha}_t} z_0 + \sqrt{1 - \bar{\alpha}_t} \epsilon, \quad \epsilon \sim \mathcal{N}(0, I), \quad \bar{\alpha}_t = \prod_{s=1}^t (1 - \beta_s).$$

When the network is trained to predict noise, the perturbed-data score is

$$s(z_t) = \nabla_z \log p_t(z_t) \approx -\frac{\epsilon_{\theta}(z_t, t)}{\sqrt{1 - \bar{\alpha}_t}}.$$

To approximate the *unperturbed* score s(z) at test time, we query a low noise level $t_{\text{noise}} \approx 0$ (we use $t_{\text{noise}} = 0$ unless stated).

Stage 2: Langevin simulation in latent space. We integrate an overdamped Langevin SDE with Euler–Maruyama, using the score as the drift:

$$z_{t+1} = z_t + T \Delta t s(z_t) + \sqrt{2T\Delta t} \eta_t, \qquad \eta_t \sim \mathcal{N}(0, \sigma_\eta^2 I).$$
 (5)

The effective diffusion variance per step is $2T \Delta t \sigma_{\eta}^2$; we set $\sigma_{\eta}=1$ unless otherwise noted. Equivalently, if $p(z) \propto \exp(-U(z)/T)$, then $Ts(z) = -\nabla U(z)$, so the drift corresponds to the gradient of an effective energy surface in latent space.

The temperature T, step size Δt , and other implementation details, such as score clipping and sampling stride are further described in Appendix A.5.

Target ensemble. Our propagators evolve only the latent coordinate z (no momenta, no barostat/box dynamics). The objective is to reproduce the *configuration-space* equilibrium of the reference MD at its thermodynamic state. Let $p_X(x)$ denote the equilibrium distribution of all-atom coordinates x from the source MD, and let $E[\cdot]$ and $D[\cdot]$ be the fixed LD-FPG encoder and decoder. The target latent law is the pushforward $p_Z = E_\# p_X$ with z = E(x) and decoded samples are $\hat{x} = D(z)$. We fit propagators so that the stationary decoded trajectory $\{\hat{x}(t)\}$ matches reference statistics in X-space (e.g., dihedral histograms, RMSF, contacts, and TM-distance free-energy surfaces). Because no Hamiltonian with momenta is integrated in latent space, we do not claim NVE energy conservation or exact physical kinetics. The score-guided Langevin propagator targets a canonical law in latent space whose invariant density is p_Z when the score is exact; Koopman and the autoregressive NN model approximate the one-step transition kernel $K(z_{t+1} | z_t)$ observed from (z_t, z_{t+1}) under the fixed encoder. Unless stated otherwise, comparisons of timescales are diagnostic rather than calibrated to wall-clock time.

4 Results and Discussion

Key result. GLDP operates reliably across scales (ADP \rightarrow 7JFL \rightarrow A₁AR) and reproduces the A₂ARactivation surface; this cross-scale pattern is the main message of the paper. See Appendix A.7 for A₁AR ablations (encoder width, pooling size, and Langevin/denoiser settings).

We first position GLDP against recent generative simulators using GLDP-NN (GLDP with the autoregressive NN propagator)(Sec. 4.1). We then compare Koopman, NN, and Langevin within the same latent space on ADP and A_1AR for stability and ensemble fidelity (Sec. 4.2, 4.3), and finally assess all three on A_2AR functional surfaces (Sec. 4.4).

4.1 Comparative Benchmarks on Trajectory Generation

To benchmark GLDP, we compared it against a diverse set of state-of-the-art models: the conceptually similar Latent Space Simulator (LSS) [4], the video-synthesis-based MD-Gen [23], and GeoTDM [45], a leading coordinate-based diffusion model. All methods were evaluated on equilibrium fidelity, flexibility, and kinetics across systems of increasing complexity: the canonical alanine dipeptide (ADP), the 7JFL protein, and the functionally complex A_1AR GPCR. The quantitative results are summarized in Table 1.

Ensemble Fidelity: We assess equilibrium fidelity via Jensen–Shannon divergence (JSD) over global coordinates and local dihedrals. On the small ADP system, GLDP attains the best coordinate JSD, while LSS edges out on backbone dihedral JSD and is closest to ground-truth RMSF. On the medium 7JFL system, MD-Gen leads on coordinate JSD and contact correlation, LSS is best on backbone-dihedral JSD, and GLDP is best on side-chain–dihedral JSD and most closely matches backbone/side-chain RMSF amplitudes. On the large GPCR A₁AR, GLDP achieves the lowest JSDs for both coordinates and dihedrals, the highest contact correlation, and the closest RMSFs, indicating the most faithful recovery of both tertiary structure and local conformational statistics. Overall, GLDP provides the strongest balance across metrics on complex proteins, while MD-Gen and LSS retain advantages on specific axes for smaller or mid-scale systems.

Molecular flexibility (RMSF). Matching the *amplitude* of motion is as important as matching mean structure, so we compare backbone/side-chain RMSF to the reference MD. On ADP, all methods undershoot side-chain flexibility; GLDP slightly overestimates backbone RMSF (0.61 Å vs. 0.56 Å), while LSS is the closest overall on ADP (0.54/0.90 Å). On 7JFL, GLDP best recovers fluctuation magnitudes for both backbone

 $^{^{1}}$ GeoTDM on 7JFL and $A_{1}AR$ exceeded 80 GB GPU memory (H100). MD-Gen does not support capped termini in our ADP setup; ADP results omitted.

Table 1: Benchmark of dynamics models. GLDP is compared against LSS, MD-Gen, and GeoTDM. Lower
JSD is better. BB: backbone; SC: sidechain. For RMSF, predicted values closer to the ground-truth row are
better. Higher contact correlation is better. Bold indicates the best result among models. N/A: not applicable.

		JSD			Avg. RN	MSF (Å)
System	Model	Dihedral (BB/SC)	Coord. (BB/SC)	Contact Corr.	Backbone	Sidechain
ADP	Ground Truth	N/A	N/A	N/A	0.56	1.34
	LSS	0.016 / N/A	0.621 / 0.633	N/A	0.54	0.90
	GeoTDM	0.123 / N/A	0.444 / 0.395	N/A	0.43	0.77
	GLDP	0.061 / N/A	0.366 / 0.386	N/A	0.61	0.89
7JFL	Ground Truth	N/A	N/A	N/A	2.09	3.05
	LSS	0.027 / 0.097	0.691 / 0.682	0.935	0.60	0.78
	MD-Gen	0.035 / 0.090	0.377 / 0.361	0.960	0.99	1.73
	GLDP	0.037 / 0.081	0.426 / 0.459	0.949	1.44	2.30
A ₁ AR	Ground Truth	N/A	N/A	N/A	1.49	1.93
	LSS	0.134 / 0.146	0.657 / 0.602	0.971	1.11	1.41
	MD-Gen	0.033 / 0.088	0.106 / 0.117	0.941	0.86	1.31
	GLDP	0.019 / 0.067	0.063 / 0.087	0.985	1.22	1.48

and side chains (1.44/2.30 Å vs. 2.09/3.05 Å), whereas MD-Gen (0.99/1.73 Å) and LSS (0.60/0.78 Å) are overly rigid. On A₁AR, all models are conservative, but GLDP remains closest to the reference variability (1.22/1.48 Å vs. 1.49/1.93 Å). In sum, GLDP most faithfully reproduces fluctuation amplitudes on the larger proteins, complementing its strong ensemble statistics.

Global contacts / long-horizon stability: As a coarse proxy for long-timescale *stability*, we compare the Pearson correlation between model and reference *time-averaged* contact maps (Appendix A.6). Contact patterns are well preserved by the top models (Pearson r > 0.93 where evaluated). On 7JFL, MD-Gen best matches the contacts (r = 0.960), while GLDP attains the highest correlation on A₁AR (r = 0.985) (ADP omitted: system too small for a meaningful contact map.)

Summary. Across flexibility and kinetics, GLDP offers an excellent balance of realism and stability. On the complex A_1AR receptor, it is the top performer across all metrics, achieving the lowest Jensen-Shannon Divergence for both coordinates and dihedrals, the highest contact correlation (r=0.985), and the most accurate fluctuation amplitudes (RMSF). This strong performance extends to other systems, where GLDP consistently places as either the best-performing model—such as for coordinate fidelity on ADP and side-chain distributions on 7JFL—or as a close competitor to the leader. Crucially, GLDP faithfully matches the flexibility of larger proteins where competing methods are often overly rigid, positioning it as a highly dependable latent-space simulator.

4.2 Long-horizon stability: autoregressive NN is most robust

Figure 2 tracks RMSD/IDDT² over rollout length and reports the *failure time* (first frame with IDDT < 0.65 relative to the initial frame). On alanine dipeptide, Koopman and the autoregressive NN remain stable for thousands of frames (failure at 4,443 and 3,176, respectively), whereas Langevin terminates early (206).

²The local Distance Difference Test (IDDT) evaluates local structural quality by measuring the preservation of inter-atomic distances.

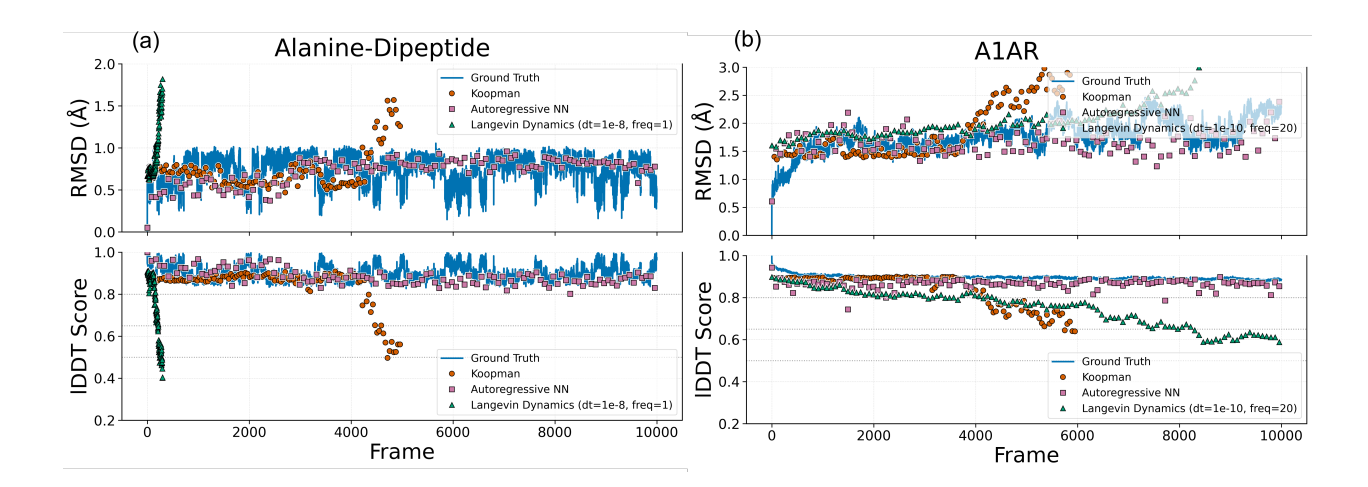


Figure 2: **Stability over long rollouts.** RMSD and lDDT versus frame index for (a) alanine dipeptide and (b) A_1AR . We define *failure time* as the first frame whose lDDT (relative to the initial frame) drops below 0.65. On A_1AR , the autoregressive NN remains stable for the entire 10,000-frame horizon (no failure), while Langevin and Koopman fail earlier; on alanine dipeptide, Koopman and NN persist for thousands of frames whereas Langevin fails early.

On A_1AR , the NN completes the full 10,000-frame horizon without failure; Langevin reaches 7,476 and Koopman 5,740. Taken together, the NN is the most robust propagator for long-horizon rollouts on both a small peptide and a large GPCR, with Koopman providing a competitive linear baseline and Langevin exhibiting sensitivity to score/integration settings.

What a "frame" means for Langevin (and how we calibrated it). For Koopman and NN, one frame equals one dataset stride $(z_t \to z_{t+1})$, so the horizontal axis matches the MD sampling stride. The Langevin propagator integrates a latent SDE with internal step size Δt and a separate sampling stride s; a plotted "frame" is a *sampled* SDE state, not a single integrator step. To make curves comparable, we calibrated $(\Delta t, s)$ to match the *short-horizon RMSD-per-frame* of the reference MD (Sec. A.5): for alanine, $\Delta t = 10^{-8}$ and s=1; for A_1AR , $\Delta t = 10^{-10}$ and s=20 (effective time per plotted frame s=3). Reported Langevin failure indices therefore count sampled outputs.

Why Langevin fails earlier on alanine. We attribute the early failure on alanine to three factors: (i) a sparsely sampled latent manifold from a large MD frame stride, yielding a rough score estimate $s(z) = \nabla_z \log p(z)$; (ii) larger apparent per-frame displacements in a tiny system (RMSD \sim 0.9 Å) making the IDDT threshold stringent; and (iii) step sizes tuned for GPCRs that are aggressive for alanine under an imperfect score, pushing the SDE off-manifold. In A₁AR, motions distribute over many atoms (IDDT penalizes less), and subsampling (s=20) further smooths per-frame jumps.

4.3 Fidelity to the Equilibrium Ensemble

We quantify ensemble fidelity by comparing free–energy surfaces (FES) of backbone (ϕ, ψ) and side–chain (χ_1, χ_2) dihedrals (Fig. 3). The Jensen–Shannon divergence (JSD) between the normalized model and reference densities serves as our primary error metric (lower is better), with all results summarized in Table 2.

Table 2: **Dihedral free-energy fidelity (JSD; lower is better).** Values computed on normalized 2D densities with periodic binning.

Propagator	$\mathbf{ADP}\ (\phi,\psi)$	$\mathbf{A_1AR}(\phi,\psi)$	$\mathbf{A_1AR}(\chi_1,\chi_2)$
Koopman	0.138	0.043	0.121
Autoreg. NN	0.061	0.019	0.067
Langevin	0.164	0.052	0.058

Backbone (ϕ, ψ) fidelity is dominated by the autoregressive NN. On backbone dihedrals, the autoregressive NN consistently outperforms the other propagators. For alanine dipeptide, the NN achieves the lowest divergence (JSD = 0.061), accurately capturing the canonical Ramachandran basins; the Koopman model's linear rigidity yields a markedly less accurate landscape (JSD = 0.138). This trend is even more pronounced on A₁AR, where the NN again produces the most faithful backbone surface (JSD = 0.019), while both Koopman and Langevin lag behind.

Side-chain (χ_1, χ_2) rotamers favor the Langevin propagator. The picture reverses for side-chain rotamers on A₁AR. Here, the score-guided *Langevin* propagator is superior, yielding the sharpest rotamer bands and the lowest JSD (0.058). This likely reflects its thermodynamically consistent drift (T s(z)) plus isotropic noise, which excels at sampling sharp, multi-modal distributions corresponding to distinct rotameric states. The NN remains close (JSD = 0.067) but slightly oversmooths high-barrier regions, whereas Koopman merges them.

Taken together, these results highlight a trade-off: the autoregressive NN excels at capturing broad backbone dynamics, while the score-guided Langevin propagator is superior for resolving fine-grained, multi-modal side-chain states.

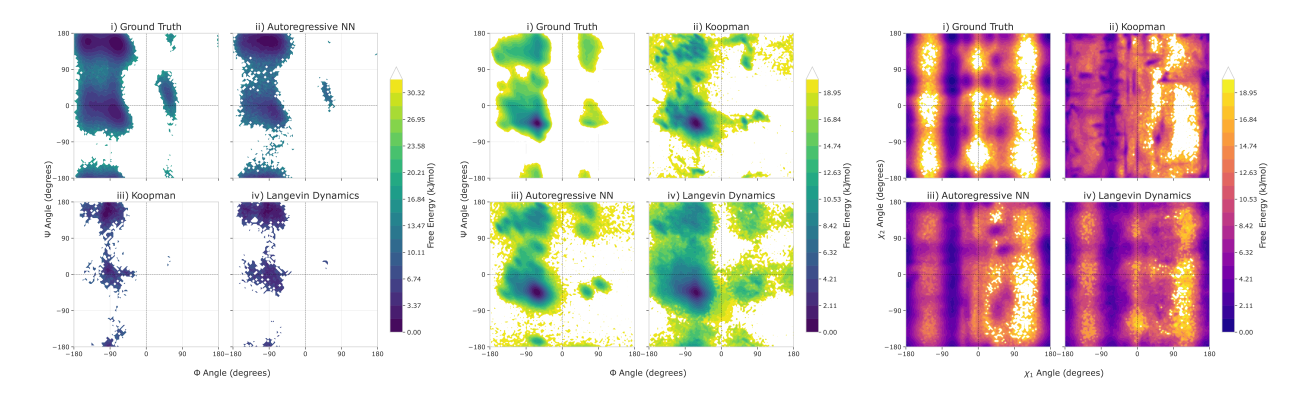


Figure 3: **Ensemble fidelity in dihedral space.** Free-energy maps for backbone (ϕ, ψ) and, for A_1AR , sidechain (χ_1, χ_2) . Alanine dipeptide (left) shows canonical basins recovered by all methods; the Autoregressive NN aligns best with the reference basin shapes. For A_1AR (middle/right), the NN most closely matches backbone structure, while the score-guided Langevin propagator recovers the sharpest rotamer bands for side-chains.

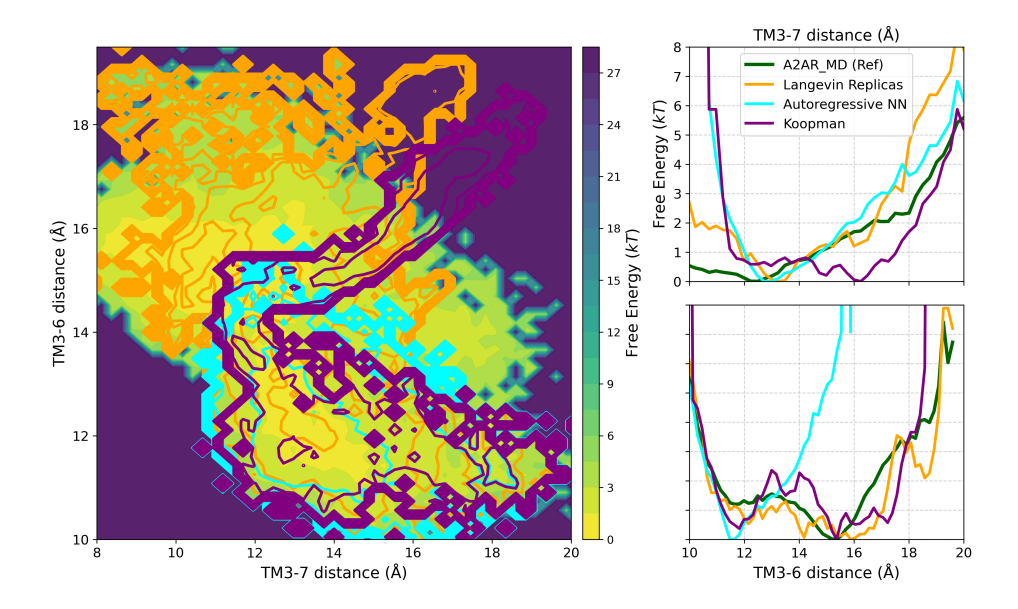


Figure 4: **Functional free-energy surface for A₂AR.** Left: 2D free energy over TM3-6 and TM3-7 distances (reference heatmap; model contours overlaid). Right: 1D profiles along each coordinate. *Langevin* spans the diagonal valley and its shoulders; the *autoregressive NN* follows the same valley with a tighter footprint; *Koopman* centers the basin but amplifies apparent barriers and reduces anisotropy. Free-energy surfaces for each propagator are averaged over 5 independent replicates.

4.4 GPCR function: activation surface in A₂AR

To assess if each propagator reproduces the inactive \leftrightarrow active switching of A₂AR, we project its dynamics onto a free-energy surface defined by the TM3-6 and TM3-7 distances (Fig. 4). These coordinates track the outward swing of TM6 and the opening of the intracellular cavity, which are hallmarks of GPCR activation (see App. Fig. 5 for representative snapshots).

A₂AR: two-dimensional surface. The reference surface forms a diagonal valley, indicating coordinated changes in TM3–6 and TM3–7 during activation. *Langevin* covers this valley most extensively, including the transition corridor connecting inactive and active-like regions. The *Autoregressive NN* follows the same valley with a tighter footprint, giving good alignment near the basin center but under-sampling the flanks. *Koopman* identifies the central basin yet shows stiffer, more isotropic contours; barriers appear sharper and the diagonal anisotropy is reduced, which limits coverage along the transition path.

One-dimensional slices. Along TM3–7 (top-right), *Langevin* and the *NN* track the position of the principal minimum and its curvature, with *Langevin* retaining broader support across the valley shoulders. *Koopman* exhibits a narrow well and steeper rise away from the minimum, consistent with its tendency to compress variance on the 2D map. Along TM3–6 (bottom-right), *Langevin* again follows the reference profile across both flanks, while the *NN* stays close near the minimum but with a slightly skewed tail. *Koopman* produces a compact basin and elevated shoulders, which reduces sampling of the transition corridor toward larger TM3–6 distances limiting its exploration of the activation corridor and showing that the non-linear propagators are more effective at tracing the complete activation pathway.

4.5 Outlook

Our comparison reveals a fundamental trade-off between the stability of data-driven models and the fine-grained physical accuracy of score-guided methods. This points toward several promising future directions. First is the development of hybrid propagators that could leverage neural networks for stable, long-horizon integration of slow collective motions while using a score-guided Langevin update for local, high-frequency side-chain sampling to ensure thermodynamic correctness. Second, a key avenue for improvement is the end-to-end training of the encoder and propagator to discover a latent representation optimized for stable temporal evolution. Such a latent space could be made more robust by enforcing thermodynamic consistency constraints or by explicitly training the model with a denoising objective, where it learns to predict the original protein structure from an input dataset to which noise has been added. For greater realism, models require rigorous kinetic calibration to match simulation or experimental timescales and should incorporate stronger physical priors like symmetry-aware (SE(3)) architectures, though their computational cost remains a significant challenge for large proteins.

Acknowledgments

A.S. was supported by a grant from the Center of Intelligence Systems (EPFL) to P.B. and P.V. This work was also supported by the Institute of Bioengineering (EPFL), the Signal Processing Laboratory (LTS2, EPFL), the Ludwig Institute for Cancer Research, and the Swiss National Science Foundation (grants 31003A_182263 and 310030_208179).

References

- [1] Ron O Dror, Daniel H Arlow, Paul Maragakis, Thomas J Mildorf, Albert C Pan, Huafeng Xu, David W Borhani, and David E Shaw. Activation mechanism of the β 2-adrenergic receptor. Proceedings of the National Academy of Sciences, 108(46):18684–18689, 2011.
- [2] Naomi R Latorraca, AJ Venkatakrishnan, and Ron O Dror. Gpcr dynamics: structures in motion. *Chemical reviews*, 117(1):139–155, 2017.
- [3] Ming Chen. Collective variable-based enhanced sampling and machine learning. *The European Physical Journal B*, 94(10):211, 2021.
- [4] Hythem Sidky, Wei Chen, and Andrew L Ferguson. Molecular latent space simulators. *Chemical Science*, 11(35):9459–9467, 2020.
- [5] Hao Wu, Andreas Mardt, Luca Pasquali, and Frank Noe. Deep generative markov state models. *Advances in Neural Information Processing Systems*, 31, 2018.
- [6] Yang Song, Jascha Sohl-Dickstein, Diederik P Kingma, Abhishek Kumar, Stefano Ermon, and Ben Poole. Score-based generative modeling through stochastic differential equations. *arXiv* preprint *arXiv*:2011.13456, 2020.
- [7] Jonathan Ho, Ajay Jain, and Pieter Abbeel. Denoising diffusion probabilistic models. *Advances in neural information processing systems*, 33:6840–6851, 2020.
- [8] Yaron Lipman, Ricky TQ Chen, Heli Ben-Hamu, Maximilian Nickel, and Matt Le. Flow matching for generative modeling. *arXiv* preprint arXiv:2210.02747, 2022.
- [9] Yann LeCun, Sumit Chopra, Raia Hadsell, M Ranzato, Fujie Huang, et al. A tutorial on energy-based learning. *Predicting structured data*, 1(0), 2006.
- [10] Marloes Arts, Victor Garcia Satorras, Chin-Wei Huang, Daniel Zugner, Marco Federici, Cecilia Clementi, Frank Noé, Robert Pinsler, and Rianne van den Berg. Two for one: Diffusion models and force fields for coarse-grained molecular dynamics. *Journal of Chemical Theory and Computation*, 19 (18):6151–6159, 2023.
- [11] Michael Plainer, Hao Wu, Leon Klein, Stephan Günnemann, and Frank Noé. Consistent sampling and simulation: Molecular dynamics with energy-based diffusion models. *arXiv preprint arXiv:2506.17139*, 2025.
- [12] Tim Hsu, Babak Sadigh, Vasily Bulatov, and Fei Zhou. Score dynamics: Scaling molecular dynamics with picoseconds time steps via conditional diffusion model. *Journal of Chemical Theory and Computation*, 20(6):2335–2348, 2024.
- [13] Shaoning Li, Yusong Wang, Mingyu Li, Jian Zhang, Bin Shao, Nanning Zheng, and Jian Tang. F3low: Frame-to-frame coarse-grained molecular dynamics with se (3) guided flow matching. *arXiv* preprint *arXiv*:2405.00751, 2024.
- [14] Bethany Lusch, J Nathan Kutz, and Steven L Brunton. Deep learning for universal linear embeddings of nonlinear dynamics. *Nature communications*, 9(1):4950, 2018.
- [15] Jonathan H Tu. *Dynamic mode decomposition: Theory and applications*. PhD thesis, Princeton University, 2013.

- [16] Carlos X Hernández, Hannah K Wayment-Steele, Mohammad M Sultan, Brooke E Husic, and Vijay S Pande. Variational encoding of complex dynamics. *Physical Review E*, 97(6):062412, 2018.
- [17] Andreas Mardt, Luca Pasquali, Hao Wu, and Frank Noé. Vampnets for deep learning of molecular kinetics. *Nature communications*, 9(1):5, 2018.
- [18] Steven L Brunton, Marko Budišić, Eurika Kaiser, and J Nathan Kutz. Modern koopman theory for dynamical systems. *arXiv preprint arXiv:2102.12086*, 2021.
- [19] Omri Azencot, N Benjamin Erichson, Vanessa Lin, and Michael Mahoney. Forecasting sequential data using consistent koopman autoencoders. In *International Conference on Machine Learning*, pages 475–485. PMLR, 2020.
- [20] Mahdi Ghorbani, Samarjeet Prasad, Jeffery B Klauda, and Bernard R Brooks. Graphvampnet, using graph neural networks and variational approach to markov processes for dynamical modeling of biomolecules. *The Journal of Chemical Physics*, 156(18), 2022.
- [21] Aditya Sengar, Ali Hariri, Daniel Probst, Patrick Barth, and Pierre Vandergheynst. Generative modeling of full-atom protein conformations using latent diffusion on graph embeddings. *arXiv preprint arXiv:2506.17064*, 2025.
- [22] Pantelis R Vlachas, Julija Zavadlav, Matej Praprotnik, and Petros Koumoutsakos. Accelerated simulations of molecular systems through learning of effective dynamics. *Journal of Chemical Theory and Computation*, 18(1):538–549, 2021.
- [23] Bowen Jing, Hannes Stärk, Tommi Jaakkola, and Bonnie Berger. Generative modeling of molecular dynamics trajectories. *Advances in Neural Information Processing Systems*, 37:40534–40564, 2024.
- [24] Simon Dobers, Hannes Stark, Xiang Fu, Dominique Beaini, and Stephan Günnemann. Latent space simulator for unveiling molecular free energy landscapes and predicting transition dynamics. In *NeurIPS* 2023 AI for Science Workshop, 2023.
- [25] Yuning Shen, Lihao Wang, Huizhuo Yuan, Yan Wang, Bangji Yang, and Quanquan Gu. Simultaneous modeling of protein conformation and dynamics via autoregression. *arXiv* preprint arXiv:2505.17478, 2025.
- [26] Guillermo Pérez-Hernández, Fabian Paul, Toni Giorgino, Gianni De Fabritiis, and Frank Noé. Identification of slow molecular order parameters for markov model construction. *The Journal of chemical physics*, 139(1), 2013.
- [27] Christoph Wehmeyer and Frank Noé. Time-lagged autoencoders: Deep learning of slow collective variables for molecular kinetics. *The Journal of chemical physics*, 148(24), 2018.
- [28] Ziyue Zou, Dedi Wang, and Pratyush Tiwary. A graph neural network-state predictive information bottleneck (gnn-spib) approach for learning molecular thermodynamics and kinetics. *Digital Discovery*, 4(1):211–221, 2025.
- [29] Jintu Zhang, Luigi Bonati, Enrico Trizio, Odin Zhang, Yu Kang, TingJun Hou, and Michele Parrinello. Descriptor-free collective variables from geometric graph neural networks. *Journal of Chemical Theory and Computation*, 20(24):10787–10797, 2024.
- [30] Dedi Wang and Pratyush Tiwary. State predictive information bottleneck. *The Journal of Chemical Physics*, 154(13), 2021.

- [31] Haochuan Chen and Christophe Chipot. Chasing collective variables using temporal data-driven strategies. *QRB discovery*, 4:e2, 2023.
- [32] Matthew O Williams, Ioannis G Kevrekidis, and Clarence W Rowley. A data–driven approximation of the koopman operator: Extending dynamic mode decomposition. *Journal of Nonlinear Science*, 25(6): 1307–1346, 2015.
- [33] Kshitij Tayal, Arvind Renganathan, Rahul Ghosh, Xiaowei Jia, and Vipin Kumar. Koopman invertible autoencoder: Leveraging forward and backward dynamics for temporal modeling. In 2023 IEEE International Conference on Data Mining (ICDM), pages 588–597. IEEE, 2023.
- [34] Indranil Nayak, Ananda Chakrabarti, Mrinal Kumar, Fernando L Teixeira, and Debdipta Goswami. Temporally-consistent koopman autoencoders for forecasting dynamical systems. *Scientific Reports*, 15 (1):22127, 2025.
- [35] Mathias Schreiner, Ole Winther, and Simon Olsson. Implicit transfer operator learning: Multiple time-resolution models for molecular dynamics. Advances in Neural Information Processing Systems, 36:36449–36462, 2023.
- [36] Sun-Ting Tsai, Eric Fields, Yijia Xu, En-Jui Kuo, and Pratyush Tiwary. Path sampling of recurrent neural networks by incorporating known physics. *Nature communications*, 13(1):7231, 2022.
- [37] Ricky TQ Chen, Yulia Rubanova, Jesse Bettencourt, and David K Duvenaud. Neural ordinary differential equations. *Advances in neural information processing systems*, 31, 2018.
- [38] Patrick Kidger, James Foster, Xuechen Li, and Terry J Lyons. Neural sdes as infinite-dimensional gans. In *International conference on machine learning*, pages 5453–5463. PMLR, 2021.
- [39] Fang Wu and Stan Z Li. Diffmd: a geometric diffusion model for molecular dynamics simulations. In *Proceedings of the AAAI conference on artificial intelligence*, volume 37, pages 5321–5329, 2023.
- [40] Jonas Kohler, Yaoyi Chen, Andreas Kramer, Cecilia Clementi, and Frank Noé. Flow-matching: Efficient coarse-graining of molecular dynamics without forces. *Journal of Chemical Theory and Computation*, 19(3):942–952, 2023.
- [41] Søren GF Rasmussen, Brian T DeVree, Yaozhong Zou, Andrew C Kruse, Ka Young Chung, Tong Sun Kobilka, Foon Sun Thian, Pil Seok Chae, Els Pardon, Diane Calinski, et al. Crystal structure of the $\beta 2$ adrenergic receptor–gs protein complex. *Nature*, 477(7366):549–555, 2011.
- [42] William I Weis and Brian K Kobilka. The molecular basis of g protein–coupled receptor activation. *Annual review of biochemistry*, 87(1):897–919, 2018.
- [43] Minkai Xu, Lantao Yu, Yang Song, Chence Shi, Stefano Ermon, and Jian Tang. Geodiff: A geometric diffusion model for molecular conformation generation. *arXiv* preprint arXiv:2203.02923, 2022.
- [44] Gabriele Corso, Hannes Stärk, Bowen Jing, Regina Barzilay, and Tommi Jaakkola. Diffdock: Diffusion steps, twists, and turns for molecular docking. *arXiv preprint arXiv:2210.01776*, 2022.
- [45] Jiaqi Han, Minkai Xu, Aaron Lou, Haotian Ye, and Stefano Ermon. Geometric trajectory diffusion models. *Advances in Neural Information Processing Systems*, 37:25628–25662, 2024.
- [46] Minkai Xu, Jiaqi Han, Aaron Lou, Jean Kossaifi, Arvind Ramanathan, Kamyar Azizzadenesheli, Jure Leskovec, Stefano Ermon, and Anima Anandkumar. Equivariant graph neural operator for modeling 3d dynamics. arXiv preprint arXiv:2401.11037, 2024.

- [47] Hao Tian, Xi Jiang, Sian Xiao, Hunter La Force, Eric C Larson, and Peng Tao. Last: Latent space-assisted adaptive sampling for protein trajectories. *Journal of chemical information and modeling*, 63 (1):67–75, 2022.
- [48] Shengchao Liu, Weitao Du, Yanjing Li, Zhuoxinran Li, Vignesh Bhethanabotla, Nakul Rampal, Omar Yaghi, Christian Borgs, Anima Anandkumar, Hongyu Guo, et al. A multi-grained symmetric differential equation model for learning protein-ligand binding dynamics. *arXiv* preprint arXiv:2401.15122, 2024.
- [49] Vincenzo Maria D'Amore, Paolo Conflitti, Luciana Marinelli, and Vittorio Limongelli. Minute-timescale free-energy calculations reveal a pseudo-active state in the adenosine a2a receptor activation mechanism. *Chem*, 10(12):3678–3698, 2024.

A Appendix

This Supplementary Information provides detailed descriptions of the models, training procedures, and evaluation metrics used in this work to ensure reproducibility.

A.1 Simulation Datasets and Code availability

The complete code, containing the pipeline to train the LD-FPG model and run GLDP, is publicly available at: https://github.com/adityasengar/GLDP. The latent trajectories used to train the propagators were derived from three publicly available Molecular Dynamics (MD) simulation datasets. For each system, the original source provided a structure file (PDB) and a coordinate trajectory (XTC). These files were then processed using the LD-FPG framework's preprocessing scripts to generate the inputs for GLDP, including a condensed.json file that provides consistent, zero-based atom indexing and defines the atom quadruplets required for calculating all backbone and side-chain dihedral angles.

Alanine Dipeptide. This dataset features N-acetyl-L-alanine-N'-methylamide, a 22-atom molecule commonly known as alanine dipeptide. It is a canonical benchmark for developing and testing new simulation methods due to its simple yet non-trivial conformational landscape, which is primarily described by its two backbone dihedral angles (ϕ, ψ) . The data was sourced from the CMB data repository at ftp.imp.fu-berlin.de and consists of a 250 ns simulation trajectory with solvent molecules removed.

7JFL (ATLAS). We use entry 7jfl_C from the ATLAS database: dsimb.inserm.fr/ATLAS/.../7jfl_C. ATLAS provides standardized all-atom, explicit-solvent MD trajectories across proteins under a common protocol.

Adenosine A₁ receptor (A₁AR). Human A₁ARtrajectories were taken from the study [49]. These are explicit-solvent, membrane-embedded GPCR simulations as described in the paper's Methods/SI and associated data records. Before encoding, we remove solvent and lipids and operate at fixed box; we assess configuration-space statistics after decoding. Where specific thermostat/barostat and T/P values are required, we defer to the original Methods/SI.

Adenosine A_{2A} **receptor** ($A_{2}AR$). $A_{2}AR$ trajectories come from the [49]. As above, simulations are explicit solvent with a membrane environment; solvent and lipids are stripped before encoding. We match configuration-space statistics to the reference ensemble and refer to the paper's Methods/SI for the exact simulation state (e.g., NVT/NPT, temperature, pressure, ions, water model, force field).

A.2 LD-FPG based Encoder-Decoder Backbone

GLDP follows an encoder-propagator-decoder blueprint. We use a fixed, pre-trained encoder-decoder from the LD-FPG model [21] and focus on comparing propagators within its learned latent space.

The latent space for this study was generated using the original LD-FPG framework. The core components are:

- Encoder: A 4-layer Chebyshev Graph Neural Network ('HNO' model) that maps all-atom coordinates $X(t) \in \mathbb{R}^{N \times 3}$ to per-atom embeddings $Z(t) \in \mathbb{R}^{N \times d_z}$.
- Pooling and Decoder: A 'ProteinStateReconstructor2D' model performs pooling on the per-atom embeddings to generate a single latent vector $z(t) \in \mathbb{R}^{d_{\text{flat}}}$ for the entire conformation. The decoder portion of this model maps this latent vector back to all-atom coordinates.

The script 'chebet_blind.py' was used to train this autoencoder and export the time-series of latent vectors $\{z_0, z_1, \ldots, z_M\}$ into an HDF5 file ('latent_reps/pooled_embedding.h5'), which serves as the ground-truth trajectory for training the propagators. Key hyperparameters for the backbone are detailed in Table 3.

Table 3: Configuration of the Pre-trained LD-FPG Backbone Model.

Component	Parameter Value
Encoder (HNO)	
Hidden Dimension (d_z)	16
Chebyshev Order (K)	4
Graph Construction	k-Nearest Neighbors ($k = 4$)
Decoder (Blind Pooling)	
Pooling Type	Blind
Pooling Output Size $(H \times W)$	50×2
Flattened Latent Dimension (d_{flat})	100 (from 50×2)
MLP Hidden Layers	12
MLP Hidden Dimension	128

Encoder (HNO). HNO denotes a Chebyshev graph neural operator: a ChebNet with polynomial filters of order K on the molecular graph (built by kNN).

Pooling. "Blind pooling" maps per–atom embeddings $Z(t) \in \mathbb{R}^{N \times d_z}$ to a fixed $H \times W$ latent by a learned MLP that aggregates across atoms without explicit residue topology; the decoder inverts this map to all-atom coordinates.

A.3 Koopman Operator Implementation Details

The Koopman operator A was computed using the fit_dmd function, which implements the standard Dynamic Mode Decomposition (DMD) algorithm. The procedure is summarized in Algorithm 1. This method provides a numerically robust way to find the best-fit linear operator A by leveraging the Singular Value Decomposition (SVD) to compute the pseudoinverse of the snapshot matrix X.

Algorithm 1 Computing the Koopman operator with (truncated) DMD

Require: Latent snapshots $\{z_t\}_{t=0}^{M-1}$, rank cap r (optional), tolerance ε (optional).

- 1: Construct $X = [z_0, \dots, z_{M-2}], Y = [z_1, \dots, z_{M-1}].$
- 2: Compute SVD: $X = U\Sigma V^{\top}$.
- 3: (Optional) choose rank r by energy or cap; set U_r, Σ_r, V_r to the top-r factors.
- 4: Form Σ_r^+ by inverting only singular values $> \varepsilon$ (set others to zero).
- 5: Compute $X^+ \leftarrow V_r \Sigma_r^+ U_r^\top$.
- 6: Set $A \leftarrow YX^+$.

Ensure: Linear propagator A (use $z_{t+1} = Az_t$, optionally with small Gaussian rollout noise).

In our implementation, the SVD truncation rank r can be set as a hyperparameter to de-noise the dynamics. If no rank is specified, the full rank of the matrix is used.

A.3.1 Koopman Propagator Hyperparameters

The SVD truncation rank (r) and the standard deviation of the Gaussian rollout noise (σ_{koop}) are key hyperparameters. They were selected independently for each system to ensure stable, long-horizon rollouts, with the final values reported in Table 4.

Table 4: Koopman	model hyperparameter	s used for each molecular system.

System	SVD Truncation Rank (r)	Rollout Noise Std. (σ_{koop})
$\overline{A_1AR}$	10	2.00×10^{-4}
Alanine Dipeptide	10	2.60×10^{-3}

A.4 Autoregressive Neural Network Details

The neural network propagator f_{θ} is implemented as a Multi-Layer Perceptron using PyTorch, as detailed in the neural_propagator.py script. The training and rollout procedures are outlined in Algorithm 2, and the specific hyperparameters are summarized in Table 5. The model is trained on a fixed percentage of the latent trajectory, with the remainder used for validation to select the best-performing model checkpoint.

Table 5: Hyperparameters for the Autoregressive NN Propagator.

Parameter	Value / Description
Architecture	
Model Type	MLP(PropagatorMLP)
Input Dimension (d_{flat})	100
Hidden Dimension	512
Hidden Layers	2
Activation Function	ReLU
Dropout Rate	0.1
Training	
Loss Function	Mean Squared Error (MSE)
Optimizer	Adam
Learning Rate	1×10^{-4}
Batch Size	128
Epochs	400
Frame Skip $(n \text{ in } z_{t+n})$	1
Training Fraction	0.8 (80% train, 20% validation)
Weight Decay	1×10^{-4}

Algorithm 2 Autoregressive NN Training and Rollout

```
Require: Latent trajectory \{z_0, \ldots, z_M\}, model f_{\theta}, learning rate \alpha.
  1: // Training
  2: Create dataset of pairs \mathcal{D} = \{(z_t, z_{t+1})\}_{t=0}^{M-2}.
  3: Initialize model parameters \theta.
  4: for each epoch do
  5:
         for each batch (z_t, z_{t+1}) in \mathcal{D} do
             Compute loss: \mathcal{L} \leftarrow ||z_{t+1} - f_{\theta}(z_t)||^2.
  6:
  7:
             Update parameters via backpropagation: \theta \leftarrow \theta - \alpha \nabla_{\theta} \mathcal{L}.
         end for
  8:
  9: end for
10:
11: // Rollout
12: Initialize trajectory: \hat{z}_0 \leftarrow z_0.
13: for t = 0, \dots, M - 2 do
         \hat{z}_{t+1} = f_{\theta}(\hat{z}_t) + \eta_t, \quad \eta_t \sim \mathcal{N}(0, \sigma_{\text{roll}}^2 I).
15: end for
Ensure: Trained model f_{\theta}, generated trajectory \{\hat{z}_t\}.
```

We choose σ_{roll} on a validation split to match the one-step latent variance of $z_{t+1} - z_t$.

The standard deviation of the rollout noise (σ_{roll}) was calibrated for each system by matching the one-step latent residual variance on a validation set, as described in the main text. The specific values used for each simulation are listed in Table 6.

Table 6: System-specific rollout noise for the Autoregressive NN propagator.

System	Rollout Noise Std. (σ_{roll})
$\overline{A_1AR}$	1.00×10^{-3}
Alanine Dipeptide	1.00×10^{-2}
7JFL	1.50×10^{-3}

A.5 Score-Guided Langevin Propagator Details

The implementation of the Score-Guided Langevin Propagator consists of two main stages.

A.5.1 Denoiser Model Training

First, a time-conditional denoising model, $\epsilon_{\theta}(z_{\tau},\tau)$, is trained on the static set of latent embeddings from the MD trajectory. This model learns to predict the noise that was added to a "clean" sample z_0 to produce a noisy sample z_{τ} at diffusion step τ . The training objective is to minimize the Mean Squared Error between the predicted noise and the true noise: $\mathcal{L} = \mathbb{E}_{t,z_0,\epsilon} \|\epsilon - \epsilon_{\theta}(\sqrt{\bar{\alpha}_{\tau}}z_0 + \sqrt{1-\bar{\alpha}_{\tau}}\epsilon,\tau)\|^2$. The key hyperparameters for this training stage are listed in Table 7.

Table 7: Hyperparameters for Denoiser Model Training.

Parameter	Value / Description	
Denoiser Model		
Model Type	Time-conditional MLP (DiffusionMLP_v2)	
Input Dimension (d_{flat})	100	
Hidden Dimension	1024	
Diffusion Schedule		
Diffusion Steps (T_{diff})	Range explored: $450 - 1600$	
Beta Schedule	Linear	
$eta_{ extsf{start}}$	Range explored: $5 \times 10^{-6} - 0.005$	
$eta_{ ext{end}}$	Range explored: $0.02 - 0.11$	
Training		
Optimizer	Adam	
Learning Rate	1×10^{-5}	
Batch Size	64	
Epochs	50,000	

A.5.2 Langevin Simulation

We approximate the score of the *unperturbed* data distribution by evaluating the model at a low, fixed noise level, τ_{noise} (e.g., $\tau=0$). The simulation then proceeds according to Algorithm 3, with simulation-specific hyperparameters listed in Table 8.

Table 8: Hyperparameters for Langevin Simulation.

Parameter	Value / Description
Integration Time Step (Δt)	Typical range: $10^{-11} - 10^{-8}$ (arbitrary units)
Temperature (T)	Typical range: $0.001 - 1.0$ (arbitrary units)
Noise Level Timestep (τ_{noise})	0 (Evaluates score at lowest noise)
Score Clipping Norm	Optional max norm to prevent instability

Algorithm 3 Score-Guided Langevin Simulation

```
Require: Pre-trained denoiser \epsilon_{\theta}, initial state z_0, time step \Delta t, temperature T, simulation steps N_{steps}.
```

- 1: Fix a low noise level for score evaluation: $\tau \leftarrow \tau_{\text{noise}}$.
- 2: Look up noise standard deviation for τ : σ_{τ} .
- 3: Initialize trajectory: $\mathcal{Z} \leftarrow \{z_0\}$.
- 4: **for** $t = 0, ..., N_{steps} 1$ **do**
- 5: // 1. Compute Score
- 6: Predict noise for the current state z_t : $\epsilon_{pred} \leftarrow \epsilon_{\theta}(z_t, \tau)$.
- 7: Calculate the score: $s(z_t) \leftarrow -\epsilon_{pred}/\sigma_{\tau}$.
- 8: (Optional) Clip score: if $||s(z_t)|| > s_{max}$, then $s(z_t) \leftarrow s(z_t) \cdot s_{max} / ||s(z_t)||$.

9:

10: **// 2. Update State**

- 11: Calculate drift: $\Delta z_{\text{drift}} \leftarrow T \Delta t \cdot s(z_t)$.
- 12: Calculate diffusion: $\Delta z_{\text{diff}} \leftarrow \sqrt{2T\Delta t} \cdot \mathcal{N}(0, I)$.
- 13: Update state: $z_{t+1} \leftarrow z_t + \Delta z_{\text{drift}} + \Delta z_{\text{diff}}$.
- 14: Append z_{t+1} to \mathcal{Z} .
- **15: end for**

Ensure: Generated trajectory \mathcal{Z} .

As noted in the main text, key parameters such as the temperature (T), time step (Δt) , and sampling stride (s) were calibrated for each system to ensure physically realistic and stable trajectories. The specific values used for each protein simulation are provided in Table 9.

Table 9: System-specific simulation parameters for the Score-Guided Langevin propagator. Temperature (T) and time step (Δt) are in latent units.

System	$\textbf{Temperature} \ (T)$	Time Step (Δt)	Total SDE Steps	Sampling Stride (s)
Alanine Dipeptide	5.0	1.0×10^{-8}	10,000	1
A_1AR	0.8	1.0×10^{-10}	100,000	20
A_2AR	0.8	1.0×10^{-10}	100,000	20

Implementation and Calibration Details. At each step of the Langevin simulation, we evaluate the score $s(z_t)$ by calling the denoiser $\epsilon_{\theta}(z_t, t_{\text{noise}})$ and dividing by $\sqrt{1-\bar{\alpha}_{t_{\text{noise}}}}$. To prevent numerical instability from rare large updates, we clip the score's L2-norm to a maximum value of c=10. We optionally subsample the simulated path by emitting one decoded frame every s SDE steps (sampling stride) to control the apparent per-frame displacement. The temperature T and step size Δt are critical hyperparameters, which we calibrate for each system to match the short-horizon decoded RMSD-per-frame of the reference MD trajectory (as described in Section 4.2). Additional training and rollout settings, including the diffusion schedule and optimizer, are also detailed in this section.

A.6 Contact map Pearson correlation

Given a topology P and a trajectory $X = \{x_t\}_{t=1}^T$, we build a $C\alpha$ -based contact map as follows. For each frame t, extract $C\alpha$ coordinates and compute the pairwise Euclidean distance matrix $D^{(t)}$ (all residues). Average over frames to obtain $\bar{D} = \frac{1}{T} \sum_{t=1}^T D^{(t)}$, then threshold at a fixed cutoff δ (8 Å by default) to form a

binary contact map $C \in \{0,1\}^{N \times N}$:

$$C_{ij} = \mathbf{1} [\bar{D}_{ij} < \delta], \qquad C_{ii} = 0 \ \forall i.$$

We construct C^{ref} and C^{mod} with the *same* cutoff and residue selection. The reported score is the Pearson correlation coefficient between the flattened matrices:

$$r = \operatorname{corr}\left(\operatorname{vec}\left(C^{\operatorname{ref}}\right), \operatorname{vec}\left(C^{\operatorname{mod}}\right)\right),$$

Implementation notes. The procedure uses MDAnalysis for I/O and atom selection (name CA); distances are computed via pdist and squareform, then averaged over frames prior to thresholding. No exclusion of near-sequence pairs (|i-j| < 3) is applied in this metric.

A.7 Ablation Studies on A₁AR

We probe three levers that materially affect A_1AR : (i) encoder per-atom width d_z , (ii) pooled latent size prior to decoding (with fixed W=2 so $d_{flat}=2H$), and (iii) Langevin/denoiser settings. We report (i) training-time losses at the level where the lever acts, and (ii) downstream accuracy via backbone/side-chain $\Delta RMSF$ (mean absolute error, Å) and lDDT failure time (first frame with lDDT < 0.65; larger is better). For long-rollout statistics we keep the autoregressive NN and Koopman unchanged and vary only the component under study.

Conventions. For Langevin rollouts, the sampling stride is s=1 (one SDE step per frame). We choose Δt by matching the *average per-frame RMSD* of the decoded trajectory to the MD reference over K=100 frames (Sec. 4.2). Unless stated: denoiser query $\tau=0$, drift clipping $||s(z)|| \le c=10$.

A.7.1 (i) Encoder per-atom width $d_z \in \{8, 16, 32\}$

Increasing d_z lowers the autoencoder validation MSE as expected, and modestly improves downstream flexibility metrics, with diminishing returns beyond d_z =16.

$\overline{d_z}$	Enc. MSE ↓	Δ RMSF _{BB} (Å) \downarrow	$\Delta \text{RMSF}_{\text{SC}} (\mathring{\text{A}}) \downarrow$	lDDT failure (frames) [†]
8	0.020	0.34	0.54	NN > 10,000 Lang 6,800 Koop 5,200
16	0.006	0.26	0.39	NN > 10,000 Lang 7,400 Koop 5,600
32	0.003	0.24	0.37	NN $>$ 10,000 Lang 7,400 Koop 5,600

[†] A₁AR, criterion IDDT < 0.65; Lang uses s=1, $\Delta t=2\times10^{-9}$ (calibrated), $\tau=0$, clip c=10.

We select d_z =16 in the main runs for a good trade-off between training cost and downstream accuracy.

A.7.2 (ii) Pooling width H with W=2 (so $d_{flat}=2H$)

Larger pooled latents reduce decoder MSE, but very large d_{flat} slightly degrades flexibility/stability, likely by making the latent stiffer to traverse with simple propagators.

$H(d_{\mathrm{flat}})$	Dec. MSE↓	Δ RMSF _{BB} (Å) \downarrow	$\Delta \text{RMSF}_{\text{SC}} (\mathring{\text{A}}) \downarrow$	lDDT fail (Lang)	lDDT fail (Koop)
20 (40)	0.43	0.31	0.49	7,100	5,400
50 (100)	0.24	0.26	0.39	7,400	5,600
80 (160)	0.21	0.30	0.46	7,000	5,500

We therefore adopt H=50 (i.e., $d_{\text{flat}}=100$) for all main results.

A.7.3 (iii) Denoiser/Langevin settings

We ablate the diffusion schedule for the denoiser (which controls score quality), the score query level τ , the clipping threshold, and the SDE step size Δt (with stride fixed to 1). Trends:

- Diffusion schedule. Linear ($\beta_{\rm start}$, $\beta_{\rm end}$, $T_{\rm diff}$) of (5×10^{-6} , 0.03, 1400) reached denoiser MSE 0.015 (best); a looser schedule (5×10^{-5} , 0.11, 450) gave 0.050 (worst). Better denoisers reduce $\Delta {\rm RMSF_{SC}}$ by ≈ 0.03 Å.
- Score query level. τ =0 outperformed a small nonzero level (τ =20) on side-chains: Δ RMSF_{SC}=0.39 Å(τ =0) vs 0.42 Å(τ =20); backbone was unchanged within 0.01 Å.
- Clipping. Max-norm clip at c=10 stabilized occasional spikes without biasing small updates; removing clip reduced the Langevin failure time from 7,400 to 6,600 frames; c=5 was slightly over-damped (failure 7,200).
- Step size. With s=1, selecting Δt by RMSD matching (Sec. 4.2) gave $\Delta t=2\times 10^{-9}$ for A₁AR. Varying Δt by $\times 2$ changed $\Delta RMSF$ values by ≤ 0.02 Å but affected failure time ($\pm 200-300$ frames).

Summary. Bigger d_z and pooled width reduce reconstruction losses as expected, but overly large pooled latents slightly worsen flexibility and stability. A well-trained denoiser with τ =0, clip c=10, and Δt calibrated by *per-frame RMSD matching* yields the best side-chain fidelity and stable long rollouts on A₁AR.

A.8 Supplementary Figures

A.9 Supplementary Tables

Table 10: Summary of notation used in the description of the propagator models.

Symbol	Description
$\overline{z_t \in \mathbb{R}^d}$	Latent space vector at time t .
$\mathbf{X}, \mathbf{Y} \in \mathbb{R}^{d \times (M-1)}$	Snapshot matrices with <i>columns</i> as time: $\mathbf{X} = [z_0, \dots, z_{M-2}], \mathbf{Y} = [z_1, \dots, z_{M-1}].$
$A \in \mathbb{R}^{d \times d}$	Koopman linear operator.
$f_{ heta}$	Autoregressive NN with parameters θ .
p(z)	Equilibrium probability distribution of the latent variable z .
$s(z) = \nabla_z \log p(z)$	Score function of the equilibrium distribution.
$\epsilon_{ heta}(z_t, au)$	Pre-trained LD-FPG diffusion model (denoiser).
$\sigma_{ au}$	Noise schedule standard deviation from the diffusion model at step τ .
Δt	Integration time step for Langevin dynamics.
T	Temperature parameter for Langevin dynamics.
η_t	Stochastic noise term, $\eta_t \sim \mathcal{N}(0, \sigma_\eta^2 I)$ (scale σ_η specified per experiment).
d_z	Per-atom encoder embedding width (ChebNet channels).
d_{flat}	Flattened pooled latent dimension after $H \times W$ pooling (here $50 \times 2 \Rightarrow d_{\text{flat}} = 100$).
d	Shorthand for d_{flat} (the flattened pooled latent dimension).

Table 11: **Glossary of Biophysical Terms.** Definitions of key concepts from molecular dynamics and structural biology used in this work, tailored for a machine learning audience.

Term	Description for an ML Audience	
Collective Variable (CV)	A low-dimensional function of atomic coordinates (e.g., a distance or angle) designed to capture a specific, slow dynamic process like protein folding. Traditional simulation methods often require pre-defining good CVs; our work uses a learned latent space to discover them automatically.	
Potential of Mean Force (PMF)	Essentially, an effective "energy landscape" for a molecule in solution. Lower values correspond to more probable (stable) conformations. It is the target distribution that score-guided Langevin dynamics aims to sample from, often visualized as a "free-energy surface".	
Dihedral Angles (ϕ, ψ, χ)	Rotational angles around covalent bonds that define the geometry of a molecule.	
	• ϕ (phi), ψ (psi): Define the rotation of the protein backbone.	
	• χ (chi): Define the rotation of the amino acid side-chains.	
	Their statistical distributions are a sensitive measure of structural fidelity.	
Ramachandran Plot	A 2D plot of the backbone dihedral angles (ϕ, ψ) . Certain regions of this plot are "allowed" based on steric constraints, leading to characteristic high-probability basins that correspond to stable secondary structures like alpha-helices and beta-sheets.	
Rotamer	A discrete, low-energy, and therefore highly probable conformation of a protein's side-chain, defined by its set of χ angles. A key test for generative models is whether they can reproduce the correct statistical distribution of these rotameric states.	
GPCR	G protein-coupled receptor. A large and important family of transmembrane proteins that act as cellular signal transducers. They are highly dynamic and switch between different functional states (e.g., inactive, active), making them an ideal and challenging test system for dynamic models.	
IDDT	local Distance Difference Test. A metric for assessing the quality of a protein structure prediction by evaluating how well local inter-atomic distances are preserved relative to a reference structure. Unlike RMSD, it is less sensitive to global rotations and more focused on local geometric accuracy.	
RMSF	Root-Mean-Square Fluctuation. For each atom, this metric calculates the standard deviation of its position over time in a simulation trajectory. It measures the "amplitude of motion" or flexibility of different parts of the protein.	

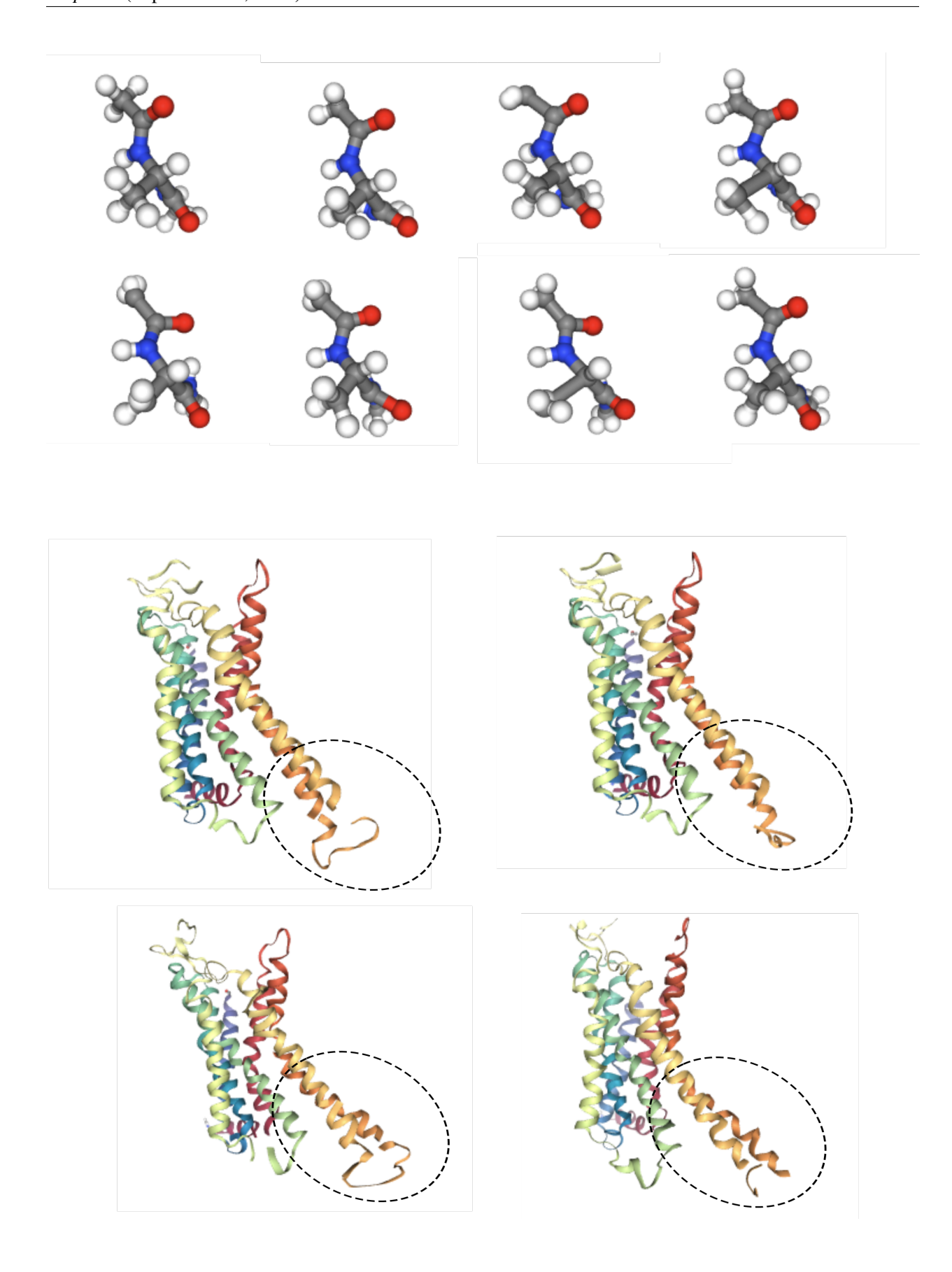


Figure 5: **Representative structural snapshots from latent rollouts.** *Top:* Alanine–dipeptide conformers sampled from a **Koopman** rollout show backbone dihedral changes across frames. *Bottom:* A₂ARsnapshots from an **Langevin** rollout; the dashed circle highlights the intracellular end of TM6, which moves outward over time—a hallmark of GPCR activation.